Global Ultrasound Elastography
in Spatial and Temporal Domains

Md Ashikuzzaman, Claudine J. Gauthier and Hassan Rivaz

Abstract—In this paper, a novel computationally efficient quasi-static ultrasound elastography technique is introduced by optimizing an energy function. Unlike conventional elastography techniques, three Radio-Frequency (RF) frames are considered to devise a non-linear cost function consisting of data-intensity similarity term, spatial regularization terms and most importantly, temporal continuity terms. We optimize the aforesaid cost function efficiently to obtain Time Delay Estimation (TDE) of all samples between the first two and last two frames of ultrasound images simultaneously, and spatially differentiate the TDE to generate axial strain map. A novelty in our spatial and temporal regularizations is that they adaptively change based on the data, which leads to substantial improvements in TDE. We handle the computational complexity resulting from incorporation of all samples from all three frames by converting our optimization problem to a sparse linear system of equations. Consideration of both spatial and temporal continuity makes the algorithm more robust to signal decorrelation than the previous algorithms. We name the proposed method GUEST: Global Ultrasound Elastography in Spatial and Temporal directions. We validated our technique with simulation, experimental phantom and *in-vivo* liver data and compare the results with two recently proposed TDE methods. In all experiments, GUEST substantially outperforms other techniques in terms of Signal to Noise Ratio (SNR), Contrast to Noise Ratio (CNR) and Strain Ratio (SR) of the strain images.

Index Terms—Real-time ultrasound elastography, Time-delay estimation, Temporal and spatial regularization, Sparse systems

I. INTRODUCTION

Ultrasound Elastography is a non-invasive medical imaging technique to infer mechanical properties of tissue by utilizing ultrasound Radio-Frequency (RF) data. Elastography is increasingly being applied in diagnosis, image-guided surgery and numerous other clinical applications [1], [2]. Among several types of clinically adopted elastography techniques, it can broadly be classified into two classes: "dynamic" which involves constant monitoring of tissue response to time-varying forces to quantify the mechanical properties of the tissue, and "quasi-static" which estimates slow deformation of tissue due to an approximately constant force [3]–[6]. Within the broad class of quasi-static elastography, our work is based on free-hand palpation elastography. Free-hand palpation elastography often suffers from decorrelation between pre- and post-compression images due to out-of-plane motion of the probe, blood flow in vessels, incoherent motion of fluid in fluid-filled lesions and the 3D nature of tissue deformation even with purely an axial probe motion [7]. Despite these drawbacks, this

Md Ashikuzzaman and Hassan Rivaz are with the Department of Electrical and Computer Engineering, Concordia University, Montreal, QC, H3G 1M8, Canada. Email: m_ashiku@encs.concordia.ca and hrivaz@ece.concordia.ca

Claudine J. Gauthier is with the Department of Physics, Concordia University, Montreal, QC, H4B 1R6, Canada. Email: claudine.gauthier@concordia.ca

method has generated interest due to its ease-of-use, since free-hand palpation elastography involves holding the probe and pressing the region of interest without requiring any additional tool [8]–[12].

Time Delay Estimation (TDE) is a necessary step in all ultrasound elastography methods. Unfortunately, TDE is an ill-posed problem because one sample of RF data by itself does not provide enough information for tracking. Therefore, two distinct classes of methods have emerged to solve this problem. In the first class, RF data is divided into several windows and it is assumed that the displacements of all samples in a particular window are same. The additional samples in the window provide enough information for tracking [13]–[17]. The second class penalizes displacement discontinuity between neighboring samples and calculates a displacement estimate for all samples of RF data. These methods are named regularized optimization-based or energy-based techniques [7], [18]–[22]. The windowing in the first class and discontinuity penalty in the second class can be considered as hard and soft regularization respectively. Between the two aforementioned techniques, window-based or block matching algorithms are more commonly used. In window-based techniques, RF data is divided into several blocks and displacement of each block is found either by looking at the maximum cross correlation [4], [23]–[26] or zero phase crossing [17], [27], [28]. Block matching algorithms make an inherent compromise between spatial resolution and accuracy based on the size of window. On the one hand, a more accurate displacement field can be obtained if the window size is ten times the ultrasound wavelength or even larger [29]. The accuracy is higher because a large correlation window reduces the estimation variance, also known as jitter error [26], [30]. Since the RF signal is non-stationary, a large window induces signal decorrelation [26], [31] and hence amplifies noise. On the other hand, better spatial resolution can be achieved by sacrificing accuracy and selecting smaller windows. The displacement estimation can be performed in either the axial direction [4], [32], [33] or both axial and lateral directions [34]–[36]. The downside of the two-dimensional search is that it is computationally more expensive. In addition, the lateral displacement field is substantially less accurate than the axial displacement field due to the low resolution of ultrasound in this direction.

TDE techniques that are based on minimization of cost functions are robust to signal decorrelation as the displacement continuity assumption is exploited to reduce estimation variance. The drawback of optimization based techniques lies in the fact that these techniques are hard to implement in real-time due to their computational complexity [20], [37]. This problem can be alleviated by using Dynamic Programming
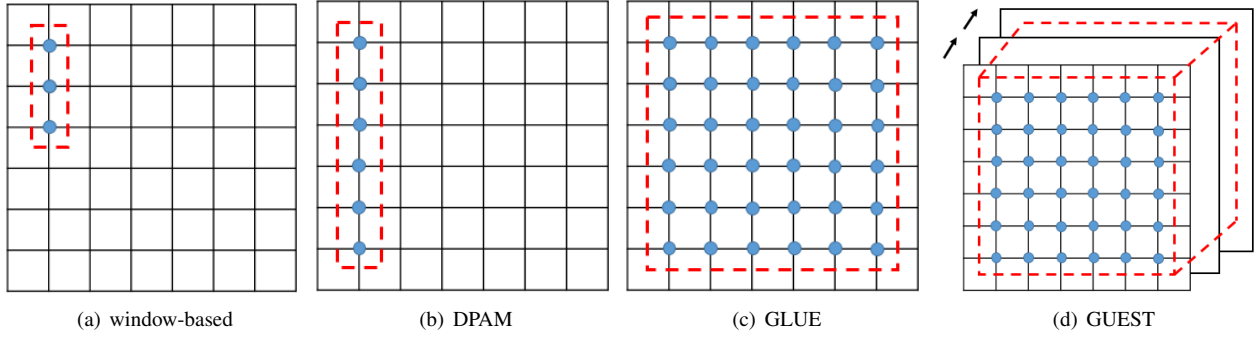
Fig. 1: Estimation of displacement field in window-based, DPAM, GLUE and GUEST algorithms. Blue dots represent samples of RF data used in displacement estimation, and the dashed window shows how the data is divided to estimate displacement fields. In (a), the data in the window is used to estimate the displacement of the central sample. In (b) and (c), displacement of all samples in an RF-line and the entire image are used, respectively, to estimate the displacement field of all these samples simultaneously. In (d), three RF frames are considered and both spatial and temporal continuity constraints are enforced. Displacement of all samples in these frames are calculated simultaneously.

(DP) [18] which efficiently calculates the integer displacement field between two RF frames. However, integer displacement field alone does not suffice for the accurate and smooth TDE requirement. Efficient minimization of a cost function involving data and displacement continuity terms to calculate the subsample displacement field was introduced in Dynamic Programming Analytic Minimization (DPAM) [7]. DPAM takes the initial integer displacement field from DP [18], and calculates the subsample axial and lateral displacements of all samples of one column of RF data. Since each column of RF data is optimized independently, discontinuity between the RF lines leads to some vertical stripes in the TDE. GLobal Ultrasound Elastography (GLUE) [19] resolved this drawback by considering the whole image for calculating the subsample displacement field. It is worth mentioning that, like DPAM, GLUE takes the initial displacement field from DP.

Though the displacement field estimated by GLUE is spatially accurate and smooth, information in the temporal domain still remains unexploited. In this paper, we introduce a novel technique called GLobal Ultrasound Elastography in Spatial and Temporal directions (GUEST) where three consecutive RF frames are incorporated instead of two to estimate the axial and lateral displacement fields. We utilize information in 3 frames, and enforce temporal continuity constraints on the displacement field to *simultaneously* estimate two 2D displacement fields. In other words, assuming that the 3 frames are I_1, I_2 and I_3, and the 2D displacement fields between I_1 and I_2 is d^1, and between I_2 and I_3 is d^2, we impose temporal constraints on d^1 and d^2. Window-based methods, DPAM, GLUE and GUEST can be summarized as follows (see also Fig. 1):

- **Window-based methods**: The displacement of each window (few ultrasound wavelengths) is calculated together.
- **DPAM**: Displacements of all samples of a single RF line are calculated together. Axial continuity is utilized to reduce estimation variance.
- **GLUE**: Displacements of all samples of a single image are calculated together. Axial and lateral continuities are

utilized to reduce estimation variance.
- **GUEST**: The displacement of all samples of multiple images is calculated together. Axial, lateral and temporal continuities are utilized to reduce estimation variance.

In addition to utilizing multiple images, another contribution of this work is the introduction of adaptive regularization terms. Instead of assuming equal displacements in the spatial domain or constant velocity in the temporal domain, we propose data-driven spatial and temporal regularization terms. Exploiting multiple images and using adaptive regularization terms leads to substantial improvements in the quality of the strain images in GUEST compared to GLUE. Specifically, adaptive spatial regularization prevents underestimation of the displacement field. Adaptive temporal regularization accounts for variations in probe velocity, which leads to different strain levels between consecutive frames. We describe these two regularization terms in Section II.B.

TDE using three images has been considered before [22]. However, there are two major differences. First, TDE optimization was limited to single RF lines like DPAM. Second, a linear stress-strain relationship was assumed, which may not always hold. GUEST is validated using simulation, phantom and *in-vivo* data, and is compared to recent window-based and optimization-based methods [14], [19]. GUEST substantially outperforms both methods in all experiments. An executable implementation of GUEST can be found at https://users.encs.concordia.ca/~hrivaz/Ultrasound_Elastography/.

An executable code of the proposed method will be available after acceptance of this paper (similar to our previous work DPAM and GLUE, which are now publicly available).

II. METHODS

Assume I_1 and I_2 are two RF frames of size $m \times n$ collected from a tissue before and after deformation respectively. Our aim is to calculate the axial and lateral displacement fields a and l which accurately map the pre-compression image I_1 to the post-compression image I_2. After finding the displacement fields, it is common to spatially differentiate them to obtain
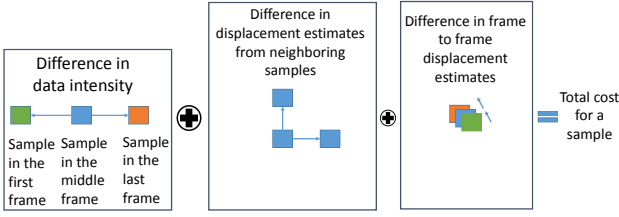
Fig. 2: An illustration of the cost function.

Fig. 3: Flow diagram demonstration of the proposed GUEST algorithm.

strain images. We first briefly explain GLUE [19], a closely related previous technique which calculates a and l. We then present GUEST and derive the mathematical equations to calculate displacement fields while enforcing spatio-temporal continuity constraints.

A. Global Time Delay Estimation (GLUE)

GLUE uses DP [18], an efficient non-iterative method for global optimization, to get initial time delay estimations in axial ($a_{i,j}$) and lateral ($l_{i,j}$) directions, where $1 \leq i \leq m$ and $1 \leq j \leq n$ denote the location in the image. DP alone provides integer displacement estimates, which is not enough to provide an accurate displacement estimation. To this end, GLUE adds subsample estimation $\Delta a(i,j)$ and $\Delta l(i,j)$ to DP displacements. $\Delta a(i,j)$ and $\Delta l(i,j)$ are obtained from the minimization of the following regularized cost function:

$$
\begin{aligned}
C(\Delta a_{1,1}, &..., \Delta a_{m,n}, \Delta l_{1,1}, ..., \Delta l_{m,n}) = \\
&\sum_{j=1}^{n}\sum_{i=1}^{m}\{[I_1(i,j) - I_2(i + a_{i,j} + \Delta a_{i,j}, j + l_{i,j} + \Delta l_{i,j})]^2 \\
&+ \alpha_1(a_{i,j} + \Delta a_{i,j} - a_{i-1,j} - \Delta a_{i-1,j})^2 \\
&+ \alpha_2(a_{i,j} + \Delta a_{i,j} - a_{i,j-1} - \Delta a_{i,j-1})^2 \\
&+ \beta_1(l_{i,j} + \Delta l_{i,j} - l_{i-1,j} - \Delta l_{i-1,j})^2 \\
&+ \beta_2(l_{i,j} + \Delta l_{i,j} - l_{i,j-1} - \Delta l_{i,j-1})^2\}
\end{aligned}
\tag{1}
$$

where α_1 and α_2 are regularization parameters for axial displacements, and β_1 and β_2 are regularization parameters for lateral displacements. By minimizing this cost function, GLUE converts the optimization problem into a linear set of equations of the classical form $Ax = b$. By solving the aforemention linear set of equations, GLUE finds the subsample displacement field and adds it to the initial estimate to obtain total displacement field.

B. GUEST: Global Ultrasound Elastography, Spatio-Temporal

We utilize three frames during tissue compression, and enforce adaptive spatio-temporal priors on the displacement field. This is in contrast to GLUE, which only considers spatial priors, and further does not adapt the priors to better represent the data. Let I_1, I_2 and I_3 be three RF frames, and a^1, l^1, a^2 and l^2 be axial and lateral DP integer displacement estimates from frame 1 to frame 2, and from frame 2 to frame 3 respectively.
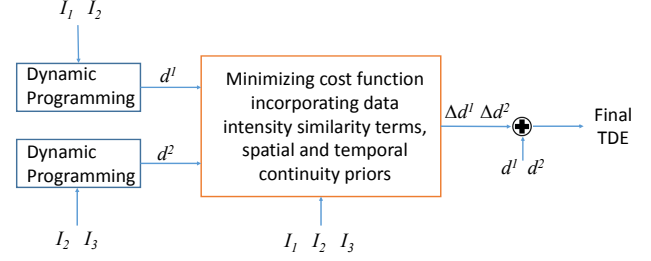
GUEST simultaneously estimates refinements Δa^1, Δl^1, Δa^2 and Δl^2 and adds them to integer DP displacement fields. To that end, we construct a cost function including data terms, spatial continuity terms and temporal continuity terms as follows (see also Fig. 2):

$$
\begin{aligned}
C(\Delta a_{1,1}^1, &\Delta l_{1,1}^1, ..., \Delta a_{m,n}^1, \Delta l_{m,n}^1, \Delta a_{1,1}^2, \Delta l_{1,1}^2, ..., \Delta a_{m,n}^2, \\
&\Delta l_{m,n}^2) = \sum_{j=1}^{n}\sum_{i=1}^{m}\{D_g + R_s + R_t\}
\end{aligned}
\tag{2}
$$

Here, D_g stands for data of the GUEST method and is defined as follows:

$$
\begin{aligned}
D_g = &[I_2(i,j) - I_1(i - a_{i,j}^1 - \Delta a_{i,j}^1, j - l_{i,j}^1 - \Delta l_{i,j}^1)]^2 \\
&+ [I_2(i,j) - I_3(i + a_{i,j}^2 + \Delta a_{i,j}^2, j + l_{i,j}^2 + \Delta l_{i,j}^2)]^2
\end{aligned}
\tag{3}
$$

R_s and R_t are adaptive spatial and temporal regularization terms respectively and are elaborated below.

1) Adaptive Spatial and Temporal Regularizations: Spatial regularization terms considered in GLUE assumed that displacement of a sample should ideally be the same as the displacement of neighbouring sample. However, this assumption is not necessarily correct in elastography. Often, such constraint results in the underestimation of the displacement field [7]. To compensate for the anticipated underestimation, we introduce adaptive spatial regularization terms of the form $\alpha(disp_i - disp_{i-1} - \epsilon)^2$ instead of $\alpha(disp_i - disp_{i-1})^2$, where ϵ is the average difference between the displacement of two neighboring pixels i and $i-1$. As such, the spatial regularization R_s is defined as follows:

$$
\begin{aligned}
R_s = &\alpha_1(a_{i,j}^1 + \Delta a_{i,j}^1 - a_{i-1,j}^1 - \Delta a_{i-1,j}^1 - \epsilon_a^1)^2 \\
&+ \alpha_1(a_{i,j}^2 + \Delta a_{i,j}^2 - a_{i-1,j}^2 - \Delta a_{i-1,j}^2 - \epsilon_a^2)^2 \\
&+ \alpha_2(a_{i,j}^1 + \Delta a_{i,j}^1 - a_{i,j-1}^1 - \Delta a_{i,j-1}^1 - \epsilon_a^1)^2 \\
&+ \alpha_2(a_{i,j}^2 + \Delta a_{i,j}^2 - a_{i,j-1}^2 - \Delta a_{i,j-1}^2 - \epsilon_a^2)^2 \\
&+ \beta_1(l_{i,j}^1 + \Delta l_{i,j}^1 - l_{i-1,j}^1 - \Delta l_{i-1,j}^1 - \epsilon_l^1)^2 \\
&+ \beta_1(l_{i,j}^2 + \Delta l_{i,j}^2 - l_{i-1,j}^2 - \Delta l_{i-1,j}^2 - \epsilon_l^2)^2 \\
&+ \beta_2(l_{i,j}^1 + \Delta l_{i,j}^1 - l_{i,j-1}^1 - \Delta l_{i,j-1}^1 - \epsilon_l^1)^2 \\
&+ \beta_2(l_{i,j}^2 + \Delta l_{i,j}^2 - l_{i,j-1}^2 - \Delta l_{i,j-1}^2 - \epsilon_l^2)^2
\end{aligned}
\tag{4}
$$

where α_1, α_2, β_1, β_2 are axial and lateral regularization weights respectively. ϵ_a^k and ϵ_l^k are axial and lateral offset terms respectively that adaptively change based on the level of strain. The superscript k is 1 when comparing I_1 to I_2, and

TABLE I: Definition of the variables, parameters, vectors and matrices

Notation	Definition	Notation	Definition
I_1, I_2, I_3	RF frames	α_3, β_3	Temporal regularization parameters
a^1, a^2	Axial displacement estimates from DP	ϵ_a^k, ϵ_l^k	Adaptive spatial regularization parameters
l^1, l^2	Lateral displacement estimates from DP	γ_a, γ_l	Adaptive temporal regularization parameters
Δa^1, Δa^2	Subsample axial displacements from GUEST	D	Matrix containing regularization parameters
Δl^1, Δl^2	Subsample Lateral displacements from GUEST	H, H_1	Matrices containing data derivatives
D_g	Data intensity similarity term	μ	Vector containing data differences
R_s	Spatial continuity term	d	Vector containing TDEs from DP
R_t	Temporal continuity term	Δd	Vector containing subsample TDEs
α_1, α_2	Axial regularization parameters	b_t	Adaptive temporal continuity vector
β_1, β_2	Lateral regularization parameters	b_s	Adaptive spatial continuity vector

is 2 when comparing I_2 to I_3. They are average difference in axial and lateral displacements between two neighboring samples and are calculated as follows:

$$\epsilon_a^k = \frac{a_m^k - a_1^k}{m-1}, \quad \epsilon_l^k = \frac{l_n^k - l_1^k}{l-1} \tag{5}$$

Before introducing the temporal regularization, it is useful to revisit some basic physics concepts. Both a and l are displacements with a unit such as mm. However, the ultrasound frame rate usually does not change during a single data collection and therefore a and l can also be considered velocity with a unit such as mm/T, where T is the time interval between two frames. Now $a^2 - a^1$ is the changes in velocity and therefore can be considered as acceleration with a unit such as mm/T^2. In free hand palpation elastography, it is unlikely that velocity of the probe is constant. Therefore, we introduce an adaptive temporal regularization that takes into account non-zero accelerations. As such, R_t is defined as:

$$R_t = \alpha_3(a_{i,j}^2 + \Delta a_{i,j}^2 - a_{i,j}^1 - \Delta a_{i,j}^1 - \gamma_a)^2 + \beta_3(l_{i,j}^2 + \Delta l_{i,j}^2 - l_{i,j}^1 - \Delta l_{i,j}^1 - \gamma_l)^2 \tag{6}$$

where, α_3 and β_3 denote temporal regularization weights in the axial and lateral directions respectively. Intuitively, instead of penalizing $a^2 - a^1$ or $l^2 - l^1$, the γ terms allow them to be different without any penalty. γ_a and γ_l approximate axial and lateral accelerations respectively and are defined as follows:

$$\gamma_a = \frac{\sum_{j=1}^{n}\sum_{i=1}^{m}\{K_g * a_{i,j}^2 - K_g * a_{i,j}^1\}}{mn}, \gamma_l = \frac{\sum_{j=1}^{n}\sum_{i=1}^{m}\{K_g * l_{i,j}^2 - K_g * l_{i,j}^1\}}{mn} \tag{7}$$

where K_g is a Gaussian kernel, which is used to average displacement estimates to obtain an estimate of acceleration with small variance.

2) Optimization of the Cost Function: R_s and R_t in (2) are quadratic in the unknowns, but the data term D_g is highly nonlinear since all the unknowns appear inside the nonlinear "functions" I_1, I_2 and I_3. Our goal is now to simplify this nonlinear function into a quadratic function by using $2D$ Taylor series expansion of the data term as follows:

$$D_g \approx \sum_{j=1}^{n}\sum_{i=1}^{m}\{[I_2(i,j) - I_1(i - a_{i,j}^1, j - l_{i,j}^1) + \Delta a_{i,j}^1 I_{1,a}^{'} + \Delta l_{i,j}^1 I_{1,l}^{'}]^2 + [I_2(i,j) - I_3(i + a_{i,j}^2, j + l_{i,j}^2) - \Delta a_{i,j}^2 I_{3,a}^{'} - \Delta l_{i,j}^2 I_{3,l}^{'}]^2\} \tag{8}$$

This equation is now quadratic in unknowns, and therefore, the cost function of Eq. 2 can be optimized by setting the partial derivatives with respect to unknowns to zero. Namely, we set $\frac{\partial C_{i,j}}{\partial \Delta a_{i,j}^1} = 0$, $\frac{\partial C_{i,j}}{\partial \Delta l_{i,j}^1} = 0$, $\frac{\partial C_{i,j}}{\partial \Delta a_{i,j}^2} = 0$ and $\frac{\partial C_{i,j}}{\partial \Delta l_{i,j}^2} = 0$ for $i = 1, 2, 3, ..., m$ and $j = 1, 2, 3, ..., n$. We organize unknown subsample displacements of $2mn$ samples in $\Delta d = [\Delta a_{1,1}^1, \Delta l_{1,1}^1, ..., \Delta a_{m,n}^1, \Delta l_{m,n}^1, \Delta a_{1,1}^2, \Delta l_{1,1}^2, ..., \Delta a_{m,n}^2, \Delta l_{m,n}^2]^T$ and the known initial estimates in $d = [a_{1,1}^1, l_{1,1}^1, ..., a_{m,n}^1, l_{m,n}^1, a_{1,1}^2, l_{1,1}^2, ..., a_{m,n}^2, l_{m,n}^2]^T$. After some algebraic operations, we get:

$$(H + D)\Delta d = H_1\mu - Dd + b_t + b_s \tag{9}$$

$H = diag(F_1, F_3)$ is a symmetric tridiagonal matrix where $F_t = diag(h_t^{'2}(1,1), h_t^{'2}(1,2), .., h_t^{'2}(m,n))$. Here, $t \in \{1, 3\}$. The entries of F_t are defined by:

$$h_t^{'2}(i,j) = \begin{bmatrix} I_{t,a}^{'2}(i,j) & I_{t,a}^{'}(i,j)I_{t,l}^{'}(i,j) \\ I_{t,a}^{'}(i,j)I_{t,l}^{'}(i,j) & I_{t,l}^{'2}(i,j) \end{bmatrix} \tag{10}$$

where $I_{t,a}^{'}(i,j)$ and $I_{t,l}^{'}(i,j)$ denote the derivatives of I_t in the axial and lateral directions at the point $(i + a_{i,j}, j + l_{i,j})$.

$H_1 = diag(F_1^{'}, F_3^{'})$ is a diagonal matrix where $F_t^{'} = diag(I_{t,a}^{'}(1,1), I_{t,l}^{'}(1,1), I_{t,a}^{'}(1,2), I_{t,l}^{'}(1,2), ..., I_{t,a}^{'}(m,n), I_{t,l}^{'}(m,n))$ and

$$\mu = \begin{bmatrix} g_1 & g_2 \end{bmatrix}^T \tag{11}$$

where

$$g_1 = \begin{bmatrix} I_2^{1,1} - I_1^{1-a_{1,1}^1, 1-l_{1,1}^1} & \cdots & I_2^{m,n} - I_1^{m-a_{m,n}^1, n-l_{m,n}^1} \end{bmatrix} \tag{12}$$

$$
Q^{'} = \begin{bmatrix}
\alpha_1 + \alpha_2 + \alpha_3 & 0 & -\alpha_2 & 0 & 0 & \dots & \dots & 0 \\
0 & \beta_1 + \beta_2 + \beta_3 & 0 & -\beta_2 & 0 & \dots & \dots & 0 \\
-\alpha_2 & 0 & \alpha_1 + 2\alpha_2 + \alpha_3 & 0 & -\alpha_2 & \ddots & \ddots & 0 \\
0 & -\beta_2 & 0 & \beta_1 + 2\beta_2 + \beta_3 & 0 & -\beta_2 & \ddots & 0 \\
\vdots & \ddots & \ddots & \ddots & \ddots & \ddots & \ddots & \vdots \\
\vdots & \ddots & \ddots & \ddots & \ddots & \ddots & \ddots & -\beta_2 \\
\vdots & \ddots & \ddots & \ddots & -\alpha_2 & 0 & \alpha_1 + \alpha_2 + \alpha_3 & 0 \\
0 & \dots & \dots & \dots & 0 & -\beta_2 & 0 & \beta_1 + \beta_2 + \beta_3
\end{bmatrix}
\tag{13}
$$

$$
R^{'} = \begin{bmatrix}
2\alpha_1 + \alpha_2 + \alpha_3 & 0 & -\alpha_2 & 0 & 0 & \dots & \dots & 0 \\
0 & 2\beta_1 + \beta_2 + \beta_3 & 0 & -\beta_2 & 0 & \dots & \dots & 0 \\
-\alpha_2 & 0 & 2\alpha_1 + 2\alpha_2 + \alpha_3 & 0 & -\alpha_2 & \ddots & \ddots & 0 \\
0 & -\beta_2 & 0 & 2\beta_1 + 2\beta_2 + \beta_3 & 0 & -\beta_2 & \ddots & 0 \\
\vdots & \ddots & \ddots & \ddots & \ddots & \ddots & \ddots & \vdots \\
\vdots & \ddots & \ddots & \ddots & \ddots & \ddots & \ddots & -\beta_2 \\
\vdots & \ddots & \ddots & \ddots & -\alpha_2 & 0 & 2\alpha_1 + \alpha_2 + \alpha_3 & 0 \\
0 & \dots & \dots & \dots & 0 & -\beta_2 & 0 & 2\beta_1 + \beta_2 + \beta_3
\end{bmatrix}
\tag{14}
$$

$$
g_2 = \begin{bmatrix} I_2^{1,1} - I_3^{1+a_{1,1}^2, 1+l_{1,1}^2} & \dots & I_2^{m,n} - I_3^{m+a_{m,n}^2, n+l_{m,n}^2} \end{bmatrix}
\tag{15}
$$

b_t, a vector of size $4mn$, is defined as:

$$
b_t = \begin{bmatrix} -\epsilon_1 & -\epsilon_2 & \dots & -\epsilon_1 & -\epsilon_2 & \epsilon_1 & \epsilon_2 & \dots & \epsilon_1 & \epsilon_2 \end{bmatrix}^T
\tag{16}
$$

where $\epsilon_1 = \alpha_3 \gamma_a$ and $\epsilon_2 = \beta_3 \gamma_l$. The adaptive regularization term b_s is defined as:

$$
b_s = \begin{bmatrix} b_1 & b_2 \end{bmatrix}^T
\tag{17}
$$

Here, b_k ($k \in \{1,2\}$) is a vector of size $2mn$. b_k is defined as:

$$
b_k = \begin{bmatrix} b_{init}^k & b_{mid}^k & \dots & b_{mid}^k & b_{end}^k \end{bmatrix}
\tag{18}
$$

b_{init}^k, b_{mid}^k and b_{end}^k are vectors of size $2n$ and are defined as follows:

$$
b_{init}^k = \begin{bmatrix} -(\alpha_1 + \alpha_2)\epsilon_a^k, -(\beta_1 + \beta_2)\epsilon_l^k, -\alpha_2 \epsilon_a^k, -\beta_2 \epsilon_l^k, \dots, \\ -\alpha_2 \epsilon_a^k, -\beta_2 \epsilon_l^k, -\alpha_1 \epsilon_a^k + \alpha_2 \epsilon_a^k, -\beta_1 \epsilon_l^k + \beta_2 \epsilon_l^k \end{bmatrix}
\tag{19}
$$

$$
b_{mid}^k = \begin{bmatrix} -\alpha_2 \epsilon_a^k & -\beta_2 \epsilon_l^k & 0 & \dots & 0 & \alpha_2 \epsilon_a^k & \beta_2 \epsilon_l^k \end{bmatrix}
\tag{20}
$$

$$
b_{end}^k = \begin{bmatrix} (\alpha_1 - \alpha_2)\epsilon_a^k, (\beta_1 - \beta_2)\epsilon_l^k, \alpha_1 \epsilon_a^k, \beta_1 \epsilon_l^k, \dots, \\ \alpha_1 \epsilon_a^k, \beta_1 \epsilon_l^k, \alpha_1 \epsilon_a^k + \alpha_2 \epsilon_a^k, \beta_1 \epsilon_l^k + \beta_2 \epsilon_l^k \end{bmatrix}
\tag{21}
$$

D is defined as:

$$
D = \begin{bmatrix} A & B \\ B & A \end{bmatrix}
\tag{22}
$$

A is:

$$
A = \begin{bmatrix}
Q^{'} & S^{'} & O^{'} & \dots & \dots & O^{'} \\
S^{'} & R^{'} & S^{'} & \ddots & \ddots & \vdots \\
O^{'} & S^{'} & R^{'} & \ddots & \ddots & \vdots \\
\vdots & \ddots & \ddots & \ddots & \ddots & \vdots \\
\vdots & \ddots & \ddots & \ddots & R^{'} & S^{'} \\
O^{'} & \dots & \dots & O^{'} & S^{'} & Q^{'}
\end{bmatrix}
\tag{23}
$$

$S^{'} = diag(-\alpha_1, -\beta_1, ..., -\alpha_1, -\beta_1)$ and $O^{'}$ is zero matrix of size $2n \times 2n$. $B = diag(S^{''}, S^{''}, ..., S^{''})$ is a diagonal matrix

of size $2mn \times 2mn$ where

$$S^{''} = diag(-\alpha_3, -\beta_3, ..., -\alpha_3, -\beta_3). \qquad (24)$$

$Q^{'}$ and $R^{'}$ are tridiagonal matrices of size $2n \times 2n$ and are defined as Eq. 13 and 14 respectively. For a quick look-up, we have provided short definitions of the variables, parameters, vectors and matrices associated with our technique in Table I. Furthermore, for a better understanding of our method, we present a flow diagram in Fig. 3.

C. Ultrasound Simulation

The simulation phantom is generated using Field II, a commonly used ultrasound image simulator [38]. Once the phantom is generated, it is compressed by ABAQUS (Province, RI), a FEM package. The mechanical property of the simulated phantom is assumed to be homogeneous with a cylindrical inclusion with an elasticity of $0\ kPa$ in the middle (i.e. a hole). The elasticity modulus of the background is considered to be $4\ kPa$. The cylindrical inclusion simulates a vein with a diameter of $8\ mm$ which easily collapses under pressure. For simulation in Field II, the parameters of the ultrasound probe are set to values consistent with a commercial probe. The frequency of the probe is $7.27MHz$, the sampling rate is $40MHz$ and the fractional bandwidth is 60%. The number of active elements for beamforming is set to 64.

III. RESULTS

For evaluating the efficacy of our algorithm, we have tested our algorithm on Finite Element Method (FEM) simulation data, a CIRS tissue-mimicking breast phantom (Norfolk,VA) and clinical data. We have compared the results with two previously published algorithms Hybrid [14] (a window-based method) and GLUE [19] (an optimization-based method). Along with qualitative comparison by inspection, we have used three conventional quality metrics Signal to Noise Ratio (SNR), Contrast to Noise Ratio (CNR) [4] and Strain Ratio (SR) to allow quantitative comparisons:

$$\text{CNR} = \frac{C}{N} = \sqrt{\frac{2(\bar{s}_b - \bar{s}_t)^2}{\sigma_b{}^2 + \sigma_t{}^2}}, \text{SNR} = \frac{\bar{s}}{\sigma}, \text{SR} = \frac{\bar{s}_t}{\bar{s}_b} \qquad (25)$$

where $\bar{s}_b$ and $\bar{s}_t$ are spatial strain average of background and target, $\sigma_b{}^2$ and $\sigma_t{}^2$ represent spatial variance of background and target, and $\bar{s}$ and σ denote spatial average and standard deviation of background window respectively. It is worth mentioning that windows where the underlying true strain is relatively uniform should be chosen to calculate SNR and CNR.

For simulation and phantom experiments, spatial regularization parameters α_1, α_2, β_1, β_2 are set to 5, 1, 5, 1 respectively. For *in-vivo* experiments, α_1 and β_1 are fixed at 20 while the other two spatial regularization parameters are kept the same. The temporal regularization parameters α_3 and β_3 are fixed at 20 for simulation and 1.5 for phantom and *in-vivo* experiments. For comparison purposes, results for GLUE and Hybrid are also generated. The tunable regularization parameters for GLUE are set to the values as described in
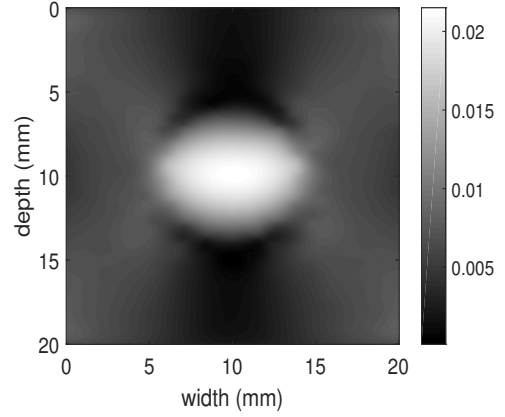

Fig. 4: Ground truth axial strain from FEM.

GLUE [19], which are also different for different applications. Ultrasound machines have presets for imaging different organs. For the Hybrid method, optimal results are obtained considering window size, inter-window shift, nearest neighbor factors and weighting factors of 380, 32, 5 and 0.4 respectively for simulation and phantom experiments. For *in-vivo* data, the Hybrid method produces optimal strain images when nearest neighbor factors are set to 3 while all other parameters are similar to those of simulation and phantom experiments. We incorporate three frames for our proposed method, and therefore have two axial strain fields. To keep the paper concise, we show only one of the strain images.

A. Simulation Results

We compress the simulation phantom by a maximum of 1% with the strain between two consecutive frames set to 0.5%. While dealing with real data, we encounter various unknown types of noise. Hence it is more realistic to add random noise to simulation RF data. We add two levels of noise with uniform distribution having Peak Signal-to-Noise Ratio (PSNR) values of $18.75\ dB$ and $10.78\ dB$. Fig. 4 shows the ground truth axial strain (i.e. the FEM strain).

Along with the results for the case of no additive noise, we report the results for the aforesaid two levels of additive noise. Fig. 5 shows the axial strain images for Hybrid, GLUE and GUEST. For all of the cases, GUEST produces visually better strain images than Hybrid and GLUE. In Fig. 5, the inclusion edge might be diffused due to two factors: first, the regularization terms in GLUE and GUEST; second, the large kernel size of the least squares method for generating strain images from displacement estimates. Table II shows the quantitative comparison of performance among the three methods. GUEST outperforms Hybrid and GLUE in terms of SNR, CNR and SR. It is worth noting that since our inclusion in this experiment is easily deformable, higher SR value corresponds to a better strain image. The target and background windows for calculating these quantitative values are demonstrated in Fig. 5(b).

To provide a more comprehensive view of CNR values, histograms are shown in Fig. 5. We have moved the small blue colored window in Fig. 5(c) within a big window to

(a) Hybrid with no additive noise

(b) GLUE with no additive noise

(c) GUEST with no additive noise

(d) Histogram of CNR values for no additive noise

(e) Hybrid with 18.75 dB PSNR

(f) GLUE with 18.75 dB PSNR

(g) GUEST with 18.75 dB PSNR

(h) Histogram of CNR values for PSNR of 18.75 dB

(i) Hybrid with 10.78 dB PSNR

(j) GLUE with 10.78 dB PSNR

(k) GUEST with 10.78 dB PSNR

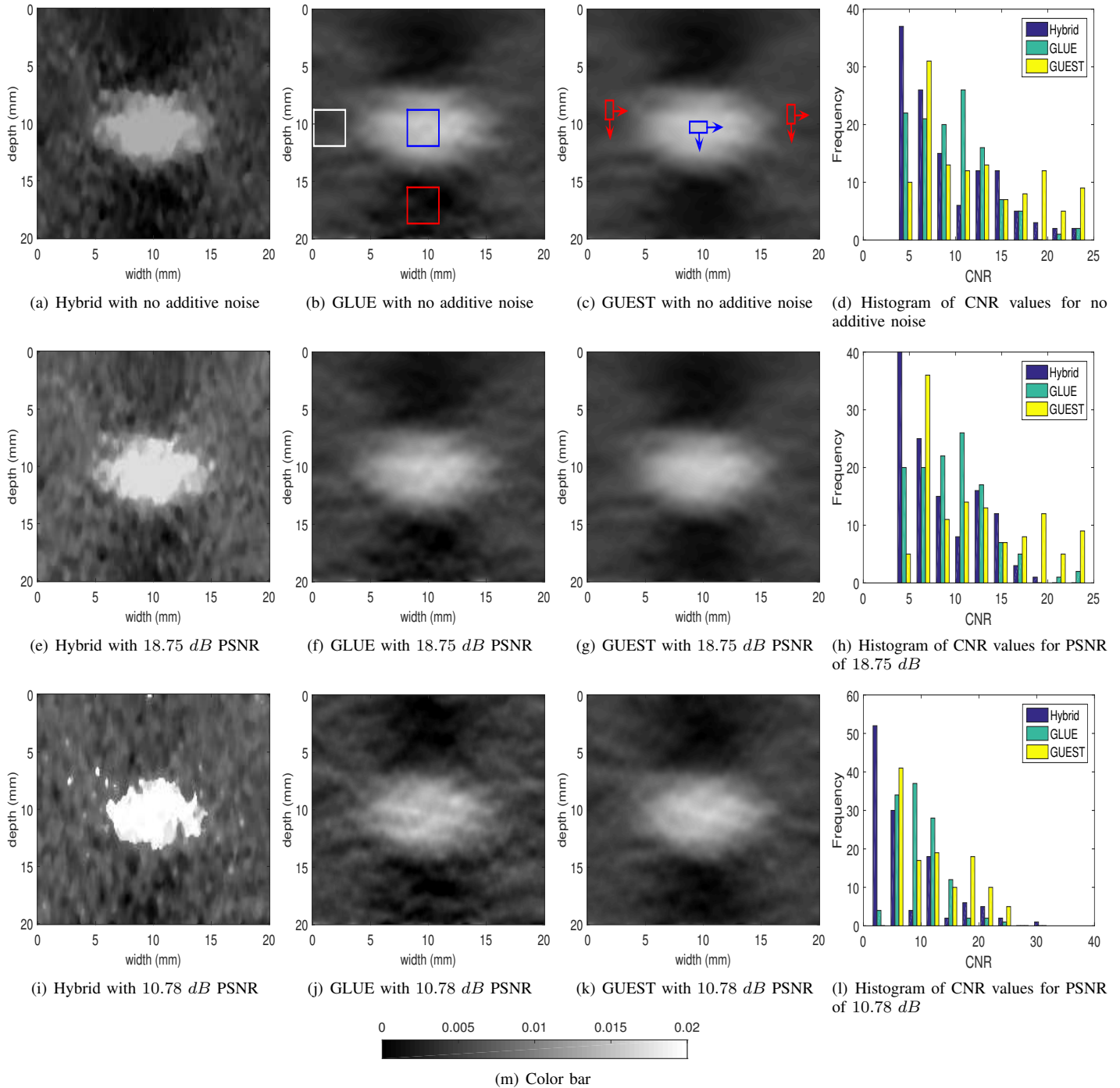(l) Histogram of CNR values for PSNR of 10.78 dB

(m) Color bar

Fig. 5: Axial strain images and histograms of CNR values for the simulation phantom. Row 1 corresponds to the case of no additive noise. Rows 2 and 3 correspond to PSNR values 18.75 dB and 10.78 dB respectively. Columns 1-3 show strain images for Hybrid, GLUE and GUEST respectively. Column 4 depicts the histograms of CNR values. (m) shows the color bar for strain images.

TABLE II: SNR, CNR and SR of the strain images for simulation phantom. CNR is calculated from blue colored target windows and red colored background windows depicted in Fig. 5(b). SR is calculated on blue colored target windows and white colored background windows. SNR is calculated on red colored background windows. Elasticity moduli of inclusion and background are 0 kPa and 4 kPa respectively.

	No additive noise			PSNR = 18.75 dB			PSNR = 10.78 dB		
	SNR	CNR	SR	SNR	CNR	SR	SNR	CNR	SR
Hybrid	1.80	16.57	**3.31**	4.15	13.07	2.53	fails	fails	fails
GLUE	1.90	17.27	2.90	1.89	15.89	2.81	1.63	13.07	2.75
GUEST	**5.72**	**23.64**	3.06	**5.09**	**23.67**	**3.00**	**2.28**	**20.02**	**3.05**

take 6 target windows. At the same time, we sweep the small red colored window within 2 large windows to consider 20 background windows. We have calculated the CNR value for every combination of target and background windows, which results in 120 total combinations. The histograms for this 120 CNR values show that, at lower CNR values, GUEST has a lower frequency than the other two algorithms under consideration. The histograms show that GUEST has much higher frequencies than Hybrid and GLUE at higher CNR values. We have performed statistical analysis using the paired t-test with the aforementioned 120 CNR values. For the case of no additive noise, GLUE is statistically better than the hybrid method with a p-value of 0.2551. For this case, GUEST is statistically better than GLUE with a p-value of 1.5458×10^{-13}. For PSNR values of 18.75 dB and 10.78 dB, GLUE is statistically better than the hybrid method with p-values of 1.6112×10^{-7} and 5.7728×10^{-10} respectively. In addition, GUEST statistically outperforms GLUE with p-values of 4.6243×10^{-10} and 1.6163×10^{-13} respectively.

B. Experimental Results

The phantom experiment was carried out at PERFORM centre, Concordia Univeristy. RF data was collected using an E-Cube R12 research ultrasound machine with an L3-12H linear array probe at the center frequency of $10MHz$ and sampling rate of $40MHz$. Clinical data was collected at Johns Hopkins Hospital from a research Antares Siemens system at $6.67MHz$ center frequency with a VF 10-5 linear array at a sampling rate of $40MHz$.

1) Phantom Results: Compression was performed on a tissue-mimicking breast phantom made from Zerdine$^{\circledR}$ (Model 059, CIRS: Tissue Simulation & Phantom Technology, Norfolk, VA) with Youngs elasticity modulus of 20 ± 5 kPa corresponding to the background, which mimics the ultrasound reflective properties of average human breast. The elasticity modulus of the spherical hard inclusion is at least twice as large as the modulus of the background. Three consecutive frames are selected to generate axial strain images. Axial strain images for phantom data are provided in Fig. 6. Quantitative values of image quality in terms of SNR, CNR and SR are represented in Table III. CNR is calculated between white colored target windows and red colored background windows, whereas SR is calculated from white colored target windows and blue colored background windows (shown in Fig. 6(b)). SNR is calculated for background windows only. It is clear that GUEST produces less noisy images with sharper edges. SNR and CNR values

TABLE III: SNR, CNR and SR of the strain images for experimental phantom. CNR is calculated from white colored target windows and red colored background windows depicted in Fig. 6(b). SR is calculated between white colored target windows and blue colored background windows. SNR is calculated on red colored background windows.

	SNR	CNR	SR
Hybrid	16.26	3.11	0.79
GLUE	15.51	5.44	0.72
GUEST	**19.91**	**6.51**	**0.65**

support our visual assessment by showing substantially higher numbers for GUEST compared to both the hybrid method and GLUE. In this experiment, the inclusion being stiffer than the background, the better strain image provides a lower SR value. Hence, according to Table III, SR values depict the fact that GUEST outperforms Hybrid and GLUE.

Similar to the simulation experiment, we have calculated CNR values for 120 combinations of target and background windows (6 target and 20 background windows) shown in Fig. 6(c). We show the histogram with the CNR values in Fig. 6(d). GUEST has higher frequency in higher CNR values and lower frequency in relatively lower CNR values. This complete quantitative analysis of the overall image shows that GUEST performs better than GLUE and Hybrid. To compare different methods, we performed paired t-test. GLUE statistically outperforms the hybrid method with p-value of 9.4008×10^{-26}. In addition, GUEST is statistically better than GLUE with p-value 2.6206×10^{-20}.

2) In-vivo Results: For the clinical study, *in-vivo* data were collected from three patients undergoing open-surgical RF thermal ablation for liver cancer at Johns Hopkins Hospital. Full details of the experimental procedure are elaborated in [7]. The study was approved by the institutional review board and informed consent was obtained from all patients. For the administration of RF ablation, RITA Model 1500 XRF generator (Rita Medical Systems, Fremont, CA) was used. The tissue was compressed simply by pushing the probe against the liver with the hand-held probe at a frequency of approximately 1 compression per 2 sec. The location of the tumor and the small surgical opening resulted in compressions with substantial out-of-plane motion of the probe. Furthermore, hepatic blood flow and other biological sources introduced additional sources of noise.

The B-mode and strain images for patient 1 are shown

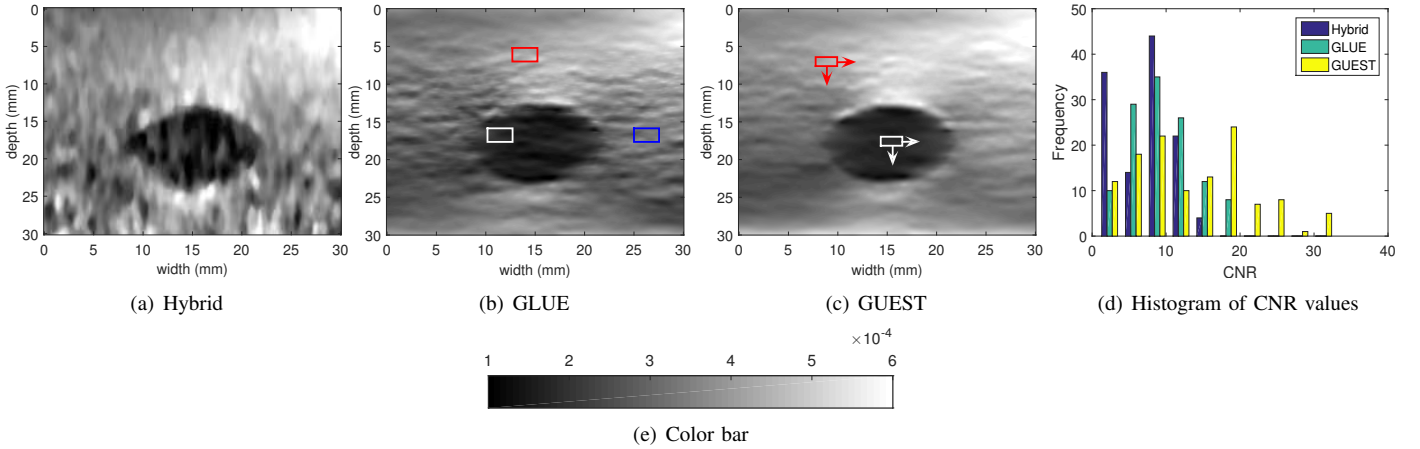(a) Hybrid   (b) GLUE   (c) GUEST   (d) Histogram of CNR values

(e) Color bar

Fig. 6: Axial strain images and histogram of CNR values for the CIRS breast elastography phantom. Columns 1 to 3 show strain images for Hybrid, GLUE and GUEST respectively. Column 4 represents the histogram of CNR values. (e) represents the color bar.

in Fig. 7. GLUE and GUEST provide substantially better visualizations of the tumor compared to the B-mode image. From Table IV, one can see that GUEST outperforms both the hybrid method and GLUE. Target and background windows for quantitative comparison are shown in Fig. 7(c). Fig. 8 presents B-mode and strain images for patient 2. The strain image from GUEST is less noisy than for the hybrid method and GLUE. Although the Hybrid method provides the most noisy strain image, it might show lesion boundary more clearly. This clearer lesion boundary could be due to the post-processing steps performed in the Hybrid method. The values in Table IV show that GUEST substantially outperforms both the hybrid method and GLUE in terms of SNR, CNR and SR. Target and background windows for calculating SNR and CNR are marked in Fig. 8(b) while target and background windows for calculating SR are indicated in Fig. 8(c).

Similar to the simulation and phantom experiments, the histogram analysis for 120 CNR values (6 blue target and 20 red background windows shown in Fig. 7(d) and Fig. 8(d)) is performed for data both from patient 1 and patient 2 (Fig. 7(e) and Fig. 8(e)). In both cases, most high CNR values are observed with GUEST. For CNR values obtained from patient 1, GLUE performs statistically better than the hybrid method with a p-value of 2.0983×10^{-23}. GUEST statistically outperforms GLUE with a p-value of 1.2734×10^{-12}. For 120 CNR values from patient 2, GLUE is statistically better than the hybrid method with a p-value of 5.2270×10^{-5}. GUEST is better than GLUE with a p-value of 2.6840×10^{-7}.

B-mode and axial strain images for patient 3 from GLUE and GUEST are depicted in Figure 9. This figure shows that GUEST provides a better visualization of the stiffer region of the tissue than GLUE. Quantitative values of SNR, CNR and SR in Table V agree with the visual assessment. Target and background windows for quantitative evaluation are shown in Fig. 9(b). As the hybrid method fails to estimate the displacement map, we report the results from GLUE and GUEST only. Histogram (Fig. 9(d)) for 120 CNR values (6 blue target and 20 red background windows shown in Fig. 9(c))

from patient 3 shows that most of the higher CNR values belong to GUEST. Statistically, GUEST is better than GLUE with a p-value of 4.9665×10^{-13}.

C. Computation Time

We have implemented our algorithm on a 4th generation 3.6 GHz Intel core-i7 PC. The other two methods (hybrid and GLUE) were also executed on the same computer. MATLAB R2015a platform was used for the implementation. For three conventional ultrasound frames of size 1000×100, the computation time of two displacement fields (frame 1 to 2 and frame 2 to 3) are reported in Table VI.

It is evident that GLUE and GUEST show much better timing performance than hybrid method. Although GUEST is slightly more expensive than GLUE, execution time can be reduced by implementing GUEST with the MATLAB MEX function. In addition to that, using GPU instead of CPU can accelerate the algorithm dramatically.

IV. DISCUSSION

It is shown in DPAM [7] and GLUE [19] that spatial regularization improves time delay estimation by reducing the effect of signal decorrelation. As ultrasound machines can collect data at a very high rate, displacement of a speckle from frame 1 to frame 2 and frame 2 to frame 3 should not be very different and hence temporal continuity is also an important property which can be utilized in improving displacement estimation.

The extent of temporal regularization is slightly tissue dependent. A rule of thumb is that a large regularization weight is needed for data collected at very high rate for imaging an organ which is expected to have a smooth displacement field. Otherwise if the tissue deforms quickly and in a complicated manner, a moderate regularization weight is preferred. In this work, the optimum value for the temporal regularization parameter was achieved by manual tuning. These values

(a) B-mode   (b) Hybrid   (c) GLUE   (d) GUEST   (e) Histogram of CNR values

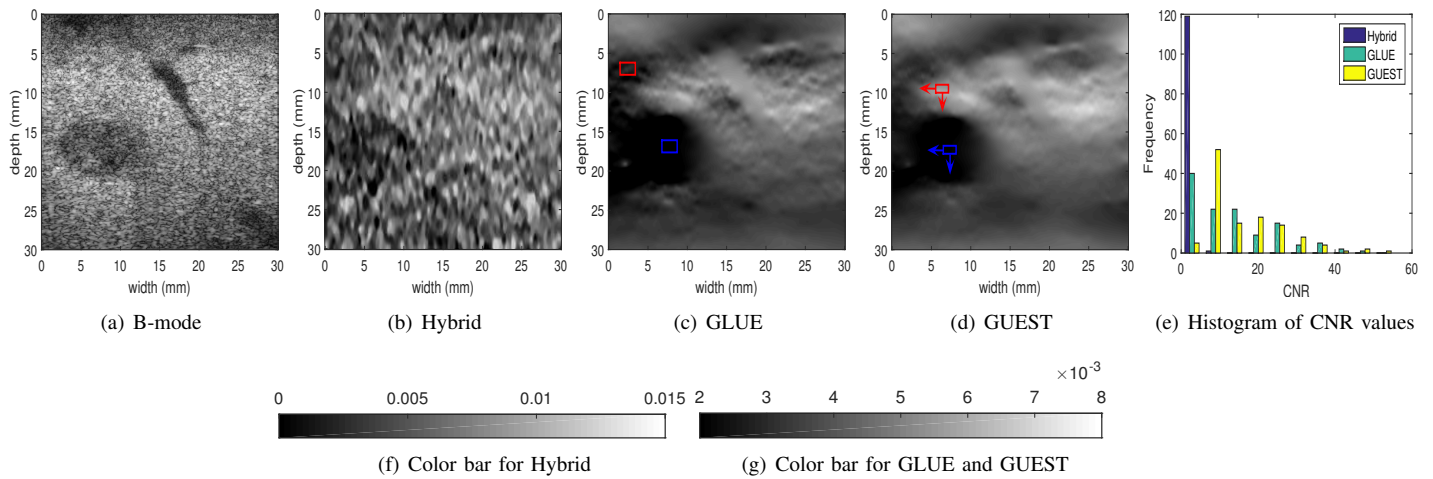(f) Color bar for Hybrid   (g) Color bar for GLUE and GUEST

Fig. 7: Results of *in-vivo* data from patient 1. (a) represents the B-mode image. (b)-(d) show strain images for Hybrid, GLUE and GUEST respectively. The tumor is clearly visible as a dark region in (c) and (d). (e) shows the histogram of CNR values. (f) represents the color bar for Hybrid whereas (g) shows the color bar for GLUE and GUEST.
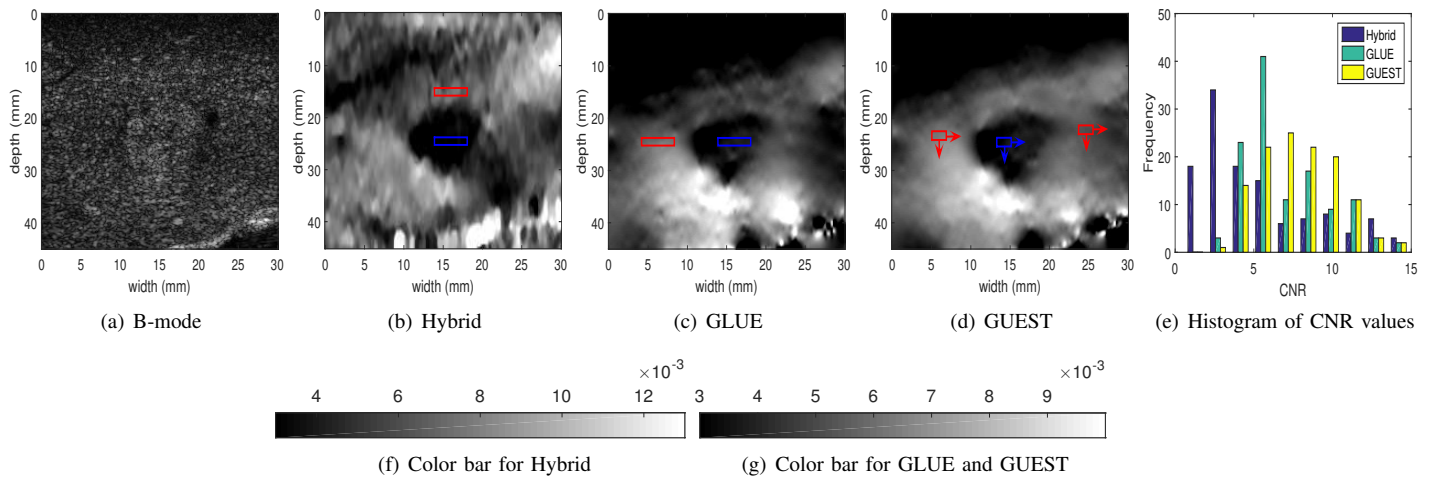

(a) B-mode   (b) Hybrid   (c) GLUE   (d) GUEST   (e) Histogram of CNR values

(f) Color bar for Hybrid   (g) Color bar for GLUE and GUEST

Fig. 8: Results of *in-vivo* data from patient 2. (a) represents the B-mode image. (b)-(d) show strain images for Hybrid, GLUE and GUEST respectively. (e) depicts the histogram of CNR values. (f) represents the color bar for Hybrid whereas (g) shows the color bar for GLUE and GUEST.

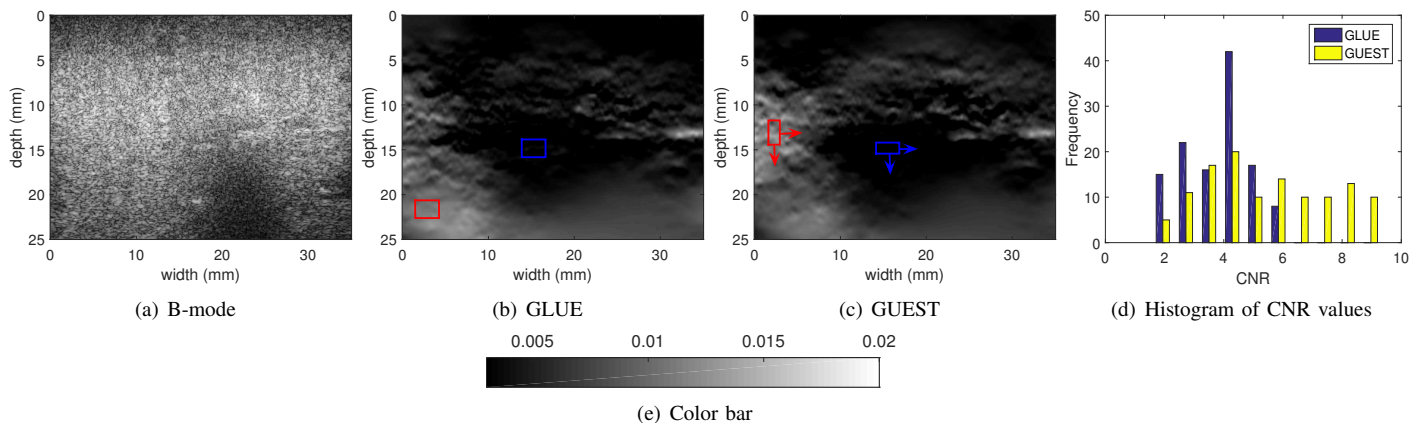(a) B-mode   (b) GLUE   (c) GUEST   (d) Histogram of CNR values

(e) Color bar

Fig. 9: Results of *in-vivo* data from patient 3. (a) represents the B-mode image. (b) and (c) show strain images for GLUE and GUEST respectively. (d) depicts the histogram of CNR values. (e) represents the color bar for strain images.

TABLE IV: SNR, CNR and SR of the strain images of patients 1 and 2. CNR and SR are calculated from blue colored target windows and red colored background windows depicted in Figs. 7(c), 8(b) and 8(c), and SNR is calculated on red colored background windows.

	Patient 1			Patient 2		
	SNR	CNR	SR	SNR	CNR	SR
Hybrid	2.18	1.16	1.50	11.36	7.78	0.98
GLUE	13.21	5.81	0.67	21.59	4.97	0.61
GUEST	**21.53**	**9.67**	**0.64**	**26.99**	**10.52**	**0.54**

TABLE V: SNR, CNR and SR of the strain images of patient 3. CNR and SR are calculated with blue colored target windows and red colored background windows depicted in Fig. 9. SNR is calculated on red colored background windows.

	SNR	CNR	SR
GLUE	21.75	10.96	0.22
GUEST	**25.09**	**14.36**	**0.14**

TABLE VI: Computation time of two displacement fields between three ultrasound frames of size 1000×100.

	Time (seconds)
Hybrid	96.91
GLUE	1.34
GUEST	1.77

can be stored for imaging different types of tissue as presets. A similar approach is commonly utilized in commercial ultrasound machines which have some imaging parameters that are embedded in the pre-settings for imaging different organs. Free-hand palpation elastography is performed by pressing the tissue with a hand-held probe, which results in probe motion in all possible six degrees of freedom (three rotations and three translations). In this paper, we select RF frames that exhibit mostly axial deformations by visual inspection. Since the probe velocity, which resembles a sinusoidal function, is not constant, the average strain levels between consecutive frames is different. This issue is addressed by making the temporal continuity term adaptive. As the difference of two consecutive initial displacement estimates is averaged over many samples using a Gaussian kernel to obtain the temporal adaptation terms, low variance estimates of the acceleration are utilized in the temporal regularization term.

As reported in [7], spatial regularization may result in underestimation of displacement field due to tissue inhomogeneity. However, this issue was not taken into account in GLUE. Adaptive spatial regularization makes the proposed method (GUEST) capable of preventing such underestimation of displacement.

Memory usage is always an important concern while dealing with ultrasound RF frames, and is even more important when more than two frames are incorporated for TDE. In our work, the coefficient matrix is of size $4mn \times 4mn$ for 3 consecutive frames of size $m \times n$, requiring a prohibitive amount of memory for RF frames of conventional size. For example, the size of the coefficient matrix will be 400000×400000

for 3 ultrasound frames of size 1000×100, which requires a memory of few hundred gigabytes. But, the matrices used in our method are band matrices whose non-zero entries are confined to diagonal bands. Hence during implementation, treating the aforementioned matrices as sparse allowed us to limit the memory requirement to approximately 100MB.

As incorporating more than two frames in ultrasound elastography is unconventional, it may advocate the impression that employment of more frames keeps improving the result. However, as more frames are included, the time-delay from the reference frame also increases which may further introduce signal decorrelation noise. Computational cost is another factor which increases substantially along with the addition of new frames. Taking these two points into consideration, the optimal number of frames is an interesting avenue of further investigation.

State-of-the-art ultrasound imaging techniques have been proposed with plane-wave imaging in several applications such as vascular and cardiac imaging. The quality of ultrasound images is usually sacrificed to some extent to achieve higher frame rates. As such, temporal regularization can be a very powerful tool for these applications to produce more accurate tracking results.

Any regularization may increase estimation bias, which may lead to strain images with lower contrast. However, the results of this paper show that GUEST maintains a bias-variance trade-off by improving both SNR and CNR. In each experiment, we calculated CNR in 120 windows and showed that GUEST provides a substantially higher CNR. In addition to this, we report results for both a soft inclusion (simulation experiment) and hard inclusions (phantom and *in-vivo* experiments). Our method obtains optimal results for both cases.

V. CONCLUSION

In this work, we proposed GUEST: Global Ultrasound Elastography in Spatial and Temporal domains. We utilized information on continuity of displacement field in the temporal direction to reduce the variance of the estimated displacement field. We used three frames of RF data to formulate a cost function that is regularized both spatially and temporally. This cost function had more than a million variables and was highly nonlinear. We simplified this complex optimization problem into a sparse linear system of equations and showed that it can be efficiently solved, which makes it an attractive technique for real-time implementation on commercial ultrasound machines. We showed using simulation, phantom and *in-vivo* experiments

that GUEST substantially outperforms two recent ultrasound elastography techniques.

ACKNOWLEDGMENT

REFERENCES

[1] J. Gennisson, T. Deffieux, M. Fink, and M. Tanter, "Ultrasound elastography: Principles and techniques," *Diagnostic and Interventional Imaging*, vol. 94, no. 5, pp. 487 – 495, 2013.

[2] T. Hall, P. E. Barboneg, A. A. Oberai, J. Jiang, J.-F. Dord, S. Goenezen, and T. Fisher, "Recent results in nonlinear strain and modulus imaging," vol. 7, pp. 313–327, 11 2011.

[3] K. J. Parker, M. M. Doyley, and D. J. Rubens, "Imaging the elastic properties of tissue: the 20 year perspective," *Physics in Medicine & Biology*, vol. 56, no. 1, p. R1, 2011.

[4] J. Ophir, S. K. Alam, B. Garra, F. Kallel, E. Konofagou, T. Krouskop, and T. Varghese, "Elastography: Ultrasonic estimation and imaging of the elastic properties of tissues," *Proceedings of the Institution of Mechanical Engineers, Part H: Journal of Engineering in Medicine*, vol. 213, no. 3, pp. 203–233, 1999.

[5] G. Treece, J. Lindop, L. Chen, J. Housden, R. Prager, and A. Gee, "Real-time quasi-static ultrasound elastography," vol. 1, pp. 540–52, 08 2011.

[6] M. Omidyeganeh, Y. Xiao, M. O. Ahmad, and H. Rivaz, "Estimation of strain elastography from ultrasound radio-frequency data by utilizing analytic gradient of the similarity metric," *IEEE Transactions on Medical Imaging*, vol. 36, no. 6, pp. 1347–1358, 2017.

[7] H. Rivaz, E. M. Boctor, M. A. Choti, and G. D. Hager, "Real-time regularized ultrasound elastography," *IEEE Transactions on Medical Imaging*, vol. 30, no. 4, pp. 928–945, 2011.

[8] K. M. Hiltawsky, M. Krger, C. Starke, L. Heuser, H. Ermert, and A. Jensen, "Freehand ultrasound elastography of breast lesions: clinical results," *Ultrasound in Medicine & Biology*, vol. 27, no. 11, pp. 1461 – 1469, 2001.

[9] M. Yamakawa, N. Nitta, T. Shiina, T. Matsumura, S. Tamano, T. Mitake, and E. Ueno, "High-speed freehand tissue elasticity imaging for breast diagnosis," vol. 42, pp. 3265–3270, 05 2003.

[10] E. Turgay, S. Salcudean, and R. Rohling, "Identifying the mechanical properties of tissue by ultrasound strain imaging," *Ultrasound in Medicine & Biology*, vol. 32, no. 2, pp. 221 – 235, 2006.

[11] A. Basarab, A. Lyshchik, and P. Delachartre, "Multi-frame motion estimation for freehand elastography and its application to thyroid tumor imaging," in *2008 5th IEEE International Symposium on Biomedical Imaging: From Nano to Macro*, 2008, pp. 532–535.

[12] X. Pan, K. Liu, J. Bai, and J. Luo, "A regularization-free elasticity reconstruction method for ultrasound elastography with freehand scan," *BioMedical Engineering OnLine*, vol. 13, no. 1, p. 132, Sep 2014.

[13] M. G. Kibria and M. K. Hasan, "A class of kernel based real-time elastography algorithms," *Ultrasonics*, vol. 61, pp. 88 – 102, 2015.

[14] A. Nahiyan and M. K. Hasan, "Hybrid algorithm for elastography to visualize both solid and fluid-filled lesions," *Ultrasound in Medicine & Biology*, vol. 41, no. 4, pp. 1058 – 1078, 2015.

[15] X. Pan, K. Liu, J. Shao, J. Gao, L. Huang, J. Bai, and J. Luo, "Performance comparison of rigid and affine models for motion estimation using ultrasound radio-frequency signals," *IEEE Transactions on Ultrasonics, Ferroelectrics, and Frequency Control*, vol. 62, no. 11, pp. 1928–1943, 2015.

[16] J. Wang, Q. Huang, and X. Zhang, "Ultrasound elastography based on the normalized cross-correlation and the pso algorithm," pp. 1131–1135, 11 2017.

[17] L. Yuan and P. C. Pedersen, "Analytical phase-tracking-based strain estimation for ultrasound elasticity," *IEEE Transactions on Ultrasonics, Ferroelectrics, and Frequency Control*, vol. 62, no. 1, pp. 185–207, 2015.

[18] H. Rivaz, E. Boctor, P. Foroughi, R. Zellars, G. Fichtinger, and G. Hager, "Ultrasound elastography: A dynamic programming approach," *IEEE Transactions on Medical Imaging*, vol. 27, no. 10, pp. 1373–1377, 2008.

[19] H. S. Hashemi and H. Rivaz, "Global time-delay estimation in ultrasound elastography," *IEEE Transactions on Ultrasonics, Ferroelectrics, and Frequency Control*, vol. 64, no. 10, pp. 1625–1636, 2017.

[20] C. Pellot-Barakat, F. Frouin, M. F. Insana, and A. Herment, "Ultrasound elastography based on multiscale estimations of regularized displacement fields," *IEEE Transactions on Medical Imaging*, vol. 23, no. 2, pp. 153–163, 2004.

[21] J. Jiang and T. J. Hall, "A generalized speckle tracking algorithm for ultrasonic strain imaging using dynamic programming," *Ultrasound in Medicine & Biology*, vol. 35, no. 11, pp. 1863 – 1879, 2009.

[22] H. Rivaz, E. M. Boctor, M. A. Choti, and G. D. Hager, "Ultrasound elastography using multiple images," *Medical Image Analysis*, vol. 18, no. 2, pp. 314 – 329, 2014.

[23] R. Zahiri-Azar and S. E. Salcudean, "Motion estimation in ultrasound images using time domain cross correlation with prior estimates," *IEEE Trans. Biomedical Engineering*, vol. 53, no. 10, pp. 1990–2000, 2006.

[24] A. Kuzmin, A. M. Zakrzewski, B. W. Anthony, and V. Lempitsky, "Multi-frame elastography using a handheld force-controlled ultrasound probe," *IEEE Transactions on Ultrasonics, Ferroelectrics, and Frequency Control*, vol. 62, no. 8, pp. 1486–1500, August 2015.

[25] A. Ramalli, O. Basset, C. Cachard, E. Boni, and P. Tortoli, "Frequency-domain-based strain estimation and high-frame-rate imaging for quasi-static elastography," *IEEE Transactions on Ultrasonics, Ferroelectrics, and Frequency Control*, vol. 59, no. 4, pp. 817–824, 2012.

[26] F. Viola and W. F. Walker, "A comparison of the performance of time-delay estimators in medical ultrasound," *IEEE Transactions on Ultrasonics, Ferroelectrics, and Frequency Control*, vol. 50, no. 4, pp. 392–401, 2003.

[27] S. R. Ara, F. Mohsin, F. Alam, S. A. Rupa, S. Y. Lee, M. K. Hasan, and R. Awwal, "Phase-based direct average strain estimation for elastography," *IEEE Transactions on Ultrasonics, Ferroelectrics, and Frequency Control*, vol. 60, no. 11, pp. 2266–2283, 2013.

[28] H. Hasegawa and H. Kanai, "Improving accuracy in estimation of artery-wall displacement by referring to center frequency of rf echo," *IEEE Transactions on Ultrasonics, Ferroelectrics, and Frequency Control*, vol. 53, no. 1, pp. 52–63, 2006.

[29] J. Grondin, E. Wan, A. Gambhir, H. Garan, and E. E. Konofagou, "Intracardiac myocardial elastography in canines and humans in vivo," *IEEE Transactions on Ultrasonics, Ferroelectrics, and Frequency Control*, vol. 62, no. 2, pp. 337–349, 2015.

[30] W. F. Walker and G. E. Trahey, "A fundamental limit on delay estimation using partially correlated speckle signals," *IEEE Transactions on Ultrasonics, Ferroelectrics, and Frequency Control*, vol. 42, no. 2, pp. 301–308, 1995.

[31] M. O'Donnell, A. R. Skovoroda, B. M. Shapo, and S. Y. Emelianov, "Internal displacement and strain imaging using ultrasonic speckle tracking," *IEEE Transactions on Ultrasonics, Ferroelectrics, and Frequency Control*, vol. 41, no. 3, pp. 314–325, 1994.

[32] R. Dickinson and C. Hill, "Measurement of soft tissue motion using correlation between a-scans," *Ultrasound in Medicine & Biology*, vol. 8, no. 3, pp. 263 – 271, 1982.

[33] M. Bilgen and M. Insana, "Deformation models and correlation analysis in elastography," vol. 99, pp. 3212–24, 06 1996.

[34] E. S. Ebbini, "Phase-coupled two-dimensional speckle tracking algorithm," *IEEE Transactions on Ultrasonics, Ferroelectrics, and Frequency Control*, vol. 53, no. 5, pp. 972–990, 2006.

[35] G. M. Treece, J. E. Lindop, A. H. Gee, and R. W. Prager, "Freehand ultrasound elastography with a 3-d probe," *Ultrasound in Medicine & Biology*, vol. 34, no. 3, pp. 463 – 474, 2008.

[36] B. H. Friemel, L. N. Bohs, and G. E. Trahey, "Relative performance of two-dimensional speckle-tracking techniques: normalized correlation, non-normalized correlation and sum-absolute-difference," in *1995 IEEE Ultrasonics Symposium. Proceedings. An International Symposium*, vol. 2, 1995, pp. 1481–1484 vol.2.

[37] E. Brusseau, J. Kybic, J. F. Deprez, and O. Basset, "2-d locally regularized tissue strain estimation from radio-frequency ultrasound images: Theoretical developments and results on experimental data," *IEEE Transactions on Medical Imaging*, vol. 27, no. 2, pp. 145–160, 2008.

[38] J. Jensen, "Field: A program for simulating ultrasound systems," *Medical and Biological Engineering and Computing*, vol. 34, pp. 351–352, 1996.